Eclética Química Journal

Original article
revista.iq.unesp.br

| Vol. 47 | special issue 1 | 2022 |

Luminescence and structural properties of $Ca_{1-x}ZrO_3:Eu_x$: An experimental and theoretical approach

Marcelo Assis[1,2+], Marisa Carvalho de Oliveira[1], Amanda Fernandes Gouveia[2,3], Lara Kelly Ribeiro[1,2], Ieda Lucia Viana Rosa[1], Renan Augusto Pontes Ribeiro[4], Juan Manuel Andrés Bort[2], Elson Longo[1]

1. Federal University of São Carlos, Center for the Development of Functional Materials, São Carlos, Brazil.
2. University Jaume I, Department of Physical and Analytical Chemistry, Castelló, Spain.
3. State University of Campinas, Institute of Chemistry, Campinas, Brazil.
4. State University of Minas Gerais, Departament of Chemistry, Divinópolis, Brazil.

+Corresponding author: Marcelo Assis, **Phone:** +55 19997347439 **Email address:** marcelostassis@gmail.com

ARTICLE INFO

Article history:
Received: July 29, 2021
Accepted: November 10, 2021
Published: April 11, 2022

Section Editors: Elson Longo and Juan Manuel Andrés Bort

Keywords:
1. perovskites
2. europium
3. phosphors
4. DFT

ABSTRACT: The influence of Eu^{3+} cations in the host matrix of $CaZrO_3$ was investigated by analyzing its luminescence and structural properties. The $Ca_{1-x}ZrO_3:Eu_x$ crystals (x = 0.01, 0.02, 0.04, and 0.08 mol%) were obtained by a simple sol-gel method followed by a soft thermal treatment without any surfactant. The structural characterization was performed at short-, medium- and long-distance to verify the effect of the dopant in the host matrix. To endorse the experimental results, first-principles calculations were performed by using the CRYSTAL program associated with the density functional theory. The luminescence profile of the sample was investigated by analyzing the excitation and emission spectrum monitoring the emission at 614 nm and excited at 394 nm, noting that the sample Eu-doped with 0.08 mol% has greater emission intensity. The color variations of the characteristic emissions of $Ca_{1-x}ZrO_3:Eu_x$ crystals were evaluated according to the Commission Internationale de L'Éclairage, observing a red shift for all Eu-doped samples. A general luminescence scheme was proposed combining the density of state and the band structure calculations.

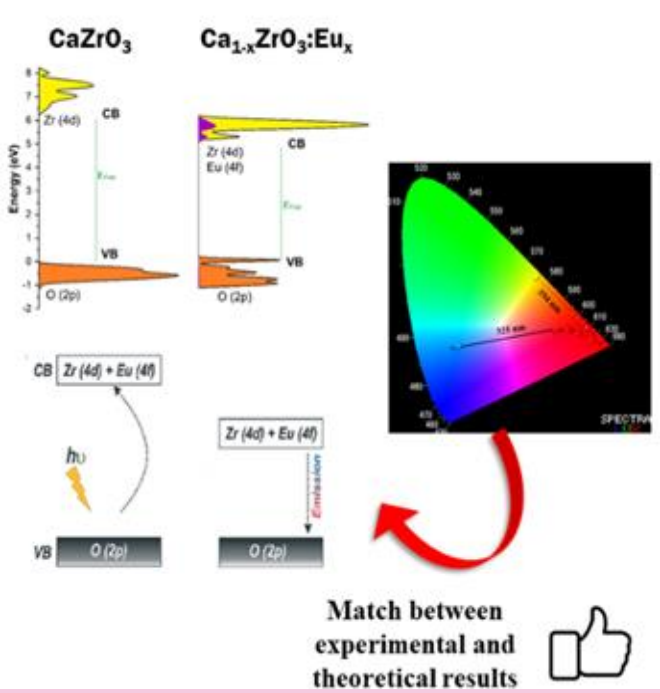

Eclética Química Journal, vol. 47, special issue 1, 2022, 90-104
ISSN: 1678-4618
DOI: 10.26850/1678-4618eqj.v47.1SI.2022.p90-104

1. Introduction

The chemical and thermal stability of materials with perovskites structure (ABO_3), such as $CaZrO_3$ (CZ), have attracted a lot of attention to be used as a host matrix for rare earth cations, thus obtaining efficient phosphors with superior luminescent activity (T. Almeida *et al*., 2021; Holzapfel *et al*., 2020; Khan *et al*., 2020; Kunti *et al*., 2021; Tian *et al*., 2020). Their properties were associated to their structural arrangement, electronic structure and the possibility to control the doping sites (A or B) (Fukushima *et al*., 2020; Navami *et al*., 2020). The crystalline lattice of the CZ is composed by distorted [ZrO_6] and [CaO_8] clusters, in which the Zr atoms are coordinated by six O atoms in an octahedral symmetry, while the Ca atoms are surrounded by eight O atoms (Eglitis *et al*., 2020; Zeba *et al*., 2020).

Rare earth cations can create new defects in the forbidden region of the band gap, modifying the electronic properties that reflect in the charge transfers process and, consequently, in the optical properties (Al Boukhari *et al*., 2020; Chu *et al*., 2020). In this way, Eu^{3+} cations have a special role for obtaining efficient red phosphors, luminescent devices and lasers, for example, from the doping of several distinct semiconductor host matrices (P. Kumar *et al*., 2021; Mazzo *et al*., 2010; 2014; Ortega *et al*., 2019; Pinatti *et al*., 2015). The applications of Eu^{3+} cations are mainly related to its nondegenerate $^7F_0$ ground state and nonoverlapping $^{2S+1}L_J$ multiplets (Targonska *et al*., 2019). These cations are sensitive to the symmetry of the local doping site and, as a consequence, can be used to identify changes in the chemical environment (Song *et al*., 2010; J. Zhang *et al*., 2020). These advantages come from its electronic configuration which also results in a pure and strong luminescence in the red region when excited in the ultraviolet (UV) region of the electromagnetic spectrum (Saif and Abdel-Mottaleb, 2007; Smith *et al*., 2019; Tymiński *et al*., 2020). These materials have too several advantages like high Stoke displacement, defined spectrum, long lifetime and high stability (Bai *et al*., 2013; Lahtinen *et al*., 2016; van der Ziel and van Uiert, 1969; Zhou *et al*., 2021).

The $Ca_{1-x}ZrO_3$:Eu_x (CZE) samples were studies in some previously published papers (Fukushima *et al*., 2020; Katyayan *et al*., 2017; S. Kumar *et al*., 2018; Shimokawa *et al*., 2015; Tiwari *et al*., 2015; H. Zhang *et al*., 2008). The method of obtaining these materials typically employ high-temperature strategies, such as sol-gel combustion method and solid-state reaction, that use temperatures above 1200 °C to not obtain secondary phases with ZrO_2 and nonstoichiometric oxides of Ca and Zr (Dubey and Tiwari, 2016; Khan *et al*., 2021; Kunti *et al*., 2021). These high temperatures also help to form a symmetrical chemical environment for the Eu^{3+} cations, increasing their luminescent emission and their lifetime decay (Fukushima *et al*., 2020; Shimokawa *et al*., 2015). Our research group is engaged in the investigation of the doping process with Eu^{3+} cations in different semiconductors (Fernandes *et al*., 2018; Lovisa *et al*., 2016; Pinatti *et al*., 2019), in particular, CZ and CZE samples were previously obtained in another experimental works (André *et al*., 2014; Oliveira *et al*., 2017; 2018; Rosa *et al*., 2015).

As a continuation of this research line, in this joint experimental and theoretical work, we reported the excitation-induced tunable photoluminescence (PL) properties of CZE, at different Eu^{3+} cations concentration (0.01, 0.02, 0.04, and 0.08 mol% named as CZE1, CZE2, CWZ4, and CZE8, respectively). The samples were prepared by a simple sol-gel method followed by a soft thermal treatment (600 °C) without any surfactant. This methodology enabled them to be promising materials in inorganic single-emitting component regions for optical applications. In addition, first-principles quantum-mechanical calculations, at the density functional theory (DFT) level, have been used to study and predict the structure and the PL, which would promote the development of CZE based phosphors.

2. Experimental procedures and computational details

Synthesis: CZ and CZE samples were prepared by the sol-gel method. The starting reagents used were calcium chloride dihydrate ($CaCl_2{\cdot}2H_2O$, 99%, Synth), zirconium oxychloride (IV) octahydrate ($ZrOCl_2{\cdot}8H_2O$, 99.5%, Sigma-Aldrich), europium oxide (Eu_2O_3, 99%, Sigma-Aldrich), ethylene glycol ($C_2H_6O_2$, 99.9%, J. T. Baker), and citric acid monohydrate ($C_6H_8O_7{\cdot}H_2O$, 99.5%, J. T. Baker). The first step of the CZ synthesis consists in the zirconium citrate's preparation. For this, 1×10^{-3} mol of $ZrOCl_2{\cdot}8H_2O$ was added to 25 mL (2.5×10^{-5} mol L^{-1}) of distilled water and add 12×10^{-3} mol of citric acid was added to the solution at 60 °C under stirring. After this process, 1×10^{-3} mol of $CaCl_2{\cdot}2H_2O$ was add to this zirconium citrate. During the previous processes, the solution was kept under N_2 bubbling to avoid the formation of unwanted phases, such as ZrO_2 and nonstoichiometric oxides of Ca and Zr. Then, ethylene glycol (in the proportion 60:40 in relation to the mass of citric acid) was added to the solution and the N_2 bubbling was removed. The temperature of the solution was changed to 80 °C to evaporate the resulting water

Eclética Química Journal, vol. 47, special issue 1, 2022, 90-104
ISSN: 1678-4618
DOI: 10.26850/1678-4618eqj.v47.1SI.2022.p90-104

and to form a resin. This resin was sent to the oven, undergoing three subsequent thermal processes, 110 °C/1 h, 250 °C/1 h and 400 °C/1 h. The resulting powder was taken to calcination at 600 °C for 1 h, obtaining a final white powder. For CZE samples, an identical process was performed, changing only that an acid solution of Eu^{3+} cations was added to the zirconium citrate before the $CaCl_2 \cdot 2H_2O$. The amount of mass of Eu^{3+} cations to obtain the replacement of Ca^{2+} by Eu^{3+} cations were carried out respecting the purity of the reagents as well as the charge balance.

Characterizations: The CZ and CZE samples were characterized by X-ray diffraction (XRD) with a Rigaku DMax 2500PC (Cu Kα λ = 1.5406 Å). Element analysis of the samples was performed with a XRF 720 Shimadzu (4 kV and 80 mA). Micro-Raman spectroscopy were performed by the iHR550 spectrometer (Horiba Jobin-Yvon) coupled to a silicon CCD detector and an argon-ion laser (Melles Griot, 514.5 nm, 200 mW). Diffuse reflectance spectroscopy (DRS) measurements were performed using a Varian Cary spectrometer model 5G in the diffuse reflectance mode, with a wavelength range of 300 to 800 nm and a scan speed of 600 nm min^{-1}. Photoluminescence measurements at room temperature were performed using a 500MSpex spectrometer coupled to a GaAs photomultiplier tube (GaAs PMT). A Kimmon He-Cd laser (325 nm laser; 40mW maximum power) was used as the excitation source for PL measurements. The Fluorolog Jobin–Yvon Fluorolog III spectrofluorometer, under excitation of a xenon lamp was used to obtain the emission (394 nm) and excitation (614 nm) spectra as well the decay lifetime.

Computational details: Computational methods and theoretical procedures were utilized to study the bulk properties of CZ and CZE structures. Calculations were carried out using the periodic ab initio CRYSTAL17 package, (Dovesi *et al.*, 2018) based on DFT using the B3LYP hybrid functional (Becke, 1993; Lee *et al.*, 1988). In all calculations, the atomic centers were described by the standard all-electron basis set for the Zr, Ca and O atoms, consisting of (9*s*)-(7631*sp*)-(621*d*), (8*s*)-(6511*sp*)-(21*d*), (8*s*)-(411*sp*)-(1*d*), respectively. Basis sets for Zr, Ca and O were taken from references (De La Pierre *et al.*, 2014; Valenzano *et al.*, 2011), whereas an effective core potential (ECP) pseudopotential, with 11 valence electrons described by (5*s*5*p*4*d*)/[3*s*3*p*3*d*] (VTZ quality) basis sets, was used for the trivalent Eu atom. According to the f-in-core approximation, the electrons of the 4f shell of Eu^{3+} are incorporated in the pseudopotential (Oliveira *et al.*, 2018).

Atomic positions and unit cell parameters were fully relaxed with respect to the total energy of the system for both CZ and CZE models. The convergence criteria for mono- and bielectronic integrals were set to 10^{-8} Hartree, while the RMS gradient, RMS displacement, maximum gradient, and maximum displacement were set to 3.0×10^{-4}, 1.2×10^{-3}, 4.5×10^{-4}, and 1.8×10^{-3} a.u., respectively. Regarding density matrix diagonalization, the reciprocal space net was described by a dense mesh consisting of a shrinking factor set to 4×4×4 in the Monkhorst–Pack method (Monkhorst and Pack, 1976). The accuracy of the evaluation of the Coulomb and exchange series was controlled by five thresholds, whose adopted values were 10^{-8}, 10^{-8}, 10^{-8}, 10^{-8} (ITOL1 to ITOL4), and 10^{-14} (ITOL5).

Herein, the CZ model was calculated considering the conventional unit cell with orthorhombic symmetry (*Pcmn*) containing 20 atoms. A supercell (2×1×2) expansion simulated the crystalline structure of the CZE model, containing 79-atoms, where two Eu^{3+} cations replaced two Ca^{2+} cations leading to the creation of one Ca^{2+} vacancy to neutralize the charges corresponding to a doping concentration of 12.5%. The neutrality in CZE model can be described as $CaZrO_3$ + Eu(III) → $Ca_{0.8125}Eu_{0.125}ZrO_3(V_{Ca})$, where V_{Ca} represents a calcium vacancy. It is worth to mention that such charge compensation mechanism is commonly used to investigate rare-earth doping in perovskites (Kunti *et al.*, 2021).

A schematic representation in terms of component clusters, the cation replacement and vacancy formation mechanisms associated with the doping process, and the crystalline structure of CZ and CZE models are illustrated in Fig. 1. Here, it is important to point out that Eu-doping configurational tests were carried out to select the most favorable sites for Eu-doping.

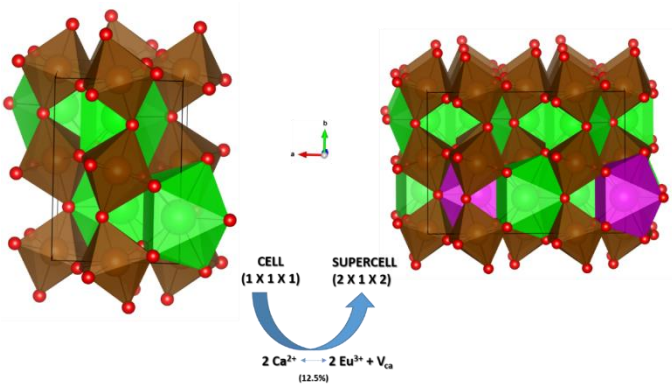

Figure 1. Schematic representation of unit cell expansion and Eu doping in CZ matrix models constructed for DFT calculations. [ZrO_6], [CaO_8] and

Eclética Química Journal, vol. 47, special issue 1, 2022, 90-104
ISSN: 1678-4618
DOI: 10.26850/1678-4618eqj.v47.1SI.2022.p90-104

[EuO_8] clusters in brown, green, and purple colors, respectively.

3. Results and Discussion

In order to understand the modifications generated at long-range in the CZ and CZE samples, XRD diffractograms were performed. XRD shows that all materials have similar profiles linked to the orthorhombic CZ structure (Fig. 2a), according to card No. 97463 in the *Inorganic Crystal Structure Database* (ICSD) (Levin *et al.*, 2003). The orthorhombic $CaZrO_3$ structure belongs to the space group *Pcmn*, being formed by distorted [CaO_8] and [ZrO_6] clusters. There was no secondary phase formation, indicating that the Eu^{3+} cations substitution process takes places successfully. For comparison, the theoretical lattice parameters and the unit cell volume calculated at the B3LYP level of theory were listed in Tab. 1.

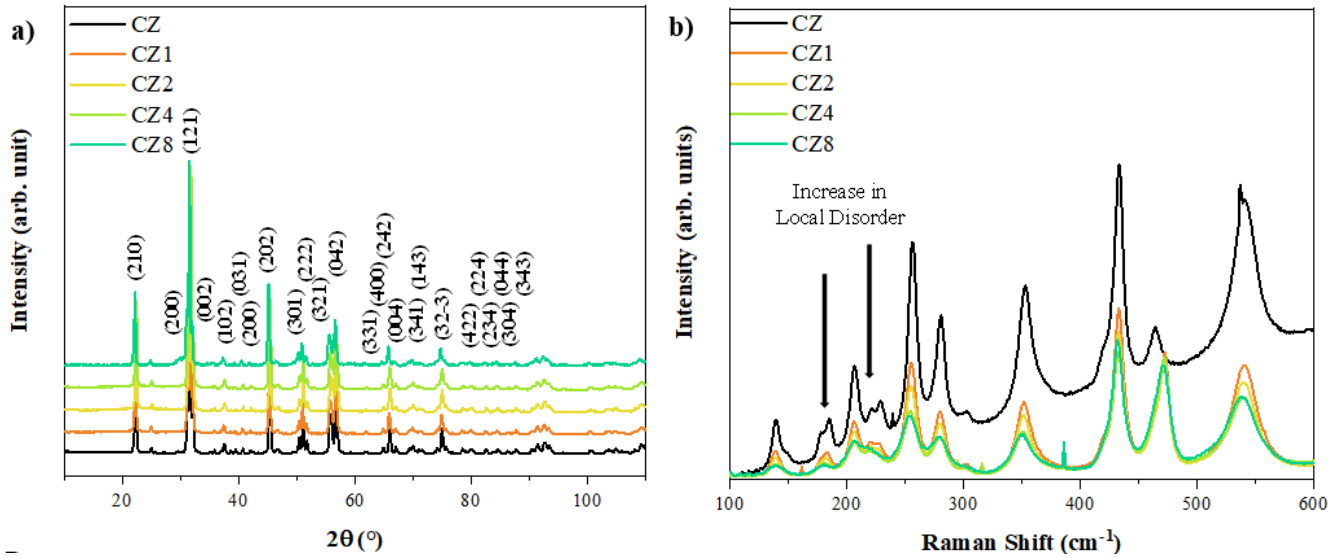

Figure 2. **(a)** X-ray diffraction and **(b)** micro-Raman spectra for CZ and CZE samples.

Table 1. Lattice parameters and unit cell volume of CZ and CZE obtained by theoretical simulations and ICSD values.

Sample	Cell Volume	Lattice Parameters		
		α = β = γ = 90° (Pcmn)		
	Å³	a (Å)	b (Å)	c (Å)
CZ	258.52	5.594	8.021	5.7611
CZE (12.5%)*	1063.72	11.322	8.069	11.641
ICSD 97463	257.45	5.583	8.007	5.759

*Corresponds to 2×1×2 conventional cells.

An analysis of the results shows that the substitution of Ca^{2+} by Eu^{3+} cations induce variations in the atomic coordinates of the O atoms, indicating the existence of structural and electronic distortions in the [CaO_8], [ZrO_6], and [EuO_8] clusters, as well as changes in the lattice parameters and an expansion of cell parameters of ~2.86% is found in the unit cell volume.

Complementing the XRD analysis, micro-Raman measurements were performed to analyze the short-range modifications caused by the substitution of Eu^{3+} cations in the CZ structure (Fig. 2b). There are 13 active modes in the Raman spectrum, which are related to specific vibrations of the [ZrO_6] clusters (André *et al.*, 2014; Evangeline *et al.*, 2017; Rosa *et al.*, 2015; Zheng *et al.*, 2004). For the CZE samples, it was observed with the increase in the concentration of Eu^{3+} cations, there is a loss of definition in the modes located at 177, 184, 205, 221, and 229 cm^{-1}. This is due to the increase in local disorder caused by the propagation of distortions of [EuO_8] clusters in the CZ structure.

The average crystallite size (D) obtained through the Scherrer's equation (Eqs. 1 and 2) and the lattice strain (ε) (Eq. 3) value are shown in Tab. 2.

$$D = \frac{0.89\lambda}{(\beta cos\theta)} \quad (1)$$

$$\beta = \sqrt{\beta_{obs}^2 - \beta_{st}^2} \quad (2)$$

$$\varepsilon = \frac{\beta}{(4tan\theta)} \quad (3)$$

where D is the average crystallite size, λ is the X-ray wavelength (0.15406 nm), θ is the Bragg angle, β_{obs} is the experimental full width at half maximum (FWHM)

Eclética Química Journal, vol. 47, special issue 1, 2022, 90-104
ISSN: 1678-4618
DOI: 10.26850/1678-4618eqj.v47.1SI.2022.p90-104

of the sample, and β_{st} is the FWHM of LaB_6 standard (Muniz *et al.*, 2016). These parameters, D and ε, were also obtained by the Williamson-Hall (WH) plot obtained through Eq. 4:

$$\frac{\beta cos\theta}{\lambda} = \frac{K}{D} + \frac{4\varepsilon}{\lambda} sen\theta \quad (4)$$

where β is the FWHM of the peak, D is the crystallite size, λ is the 0.154056 nm, K is 0.89, and ε is the lattice strain (Manohar *et al.*, 2021; Mesquita *et al.*, 2021).

For the CZE samples, a tendency to decrease the D value is observed in reference to the CZ sample. This behavior is due to the low concentrations of the rare earth that can inhibit the growth of CZ crystallite (El-Bahy *et al.*, 2009; Jayachandraiah *et al.*, 2015). In general, the doping process induces a structural and electronic strain in the crystalline lattice, evidenced by the increase in the ε value (W. Liu *et al.*, 2017). To confirm the amount of Eu^{3+} cations in the CZE samples (spectral line Lα, energy 5.849 keV), X-ray fluorescence (XRF) measurements (S4 Pioneer, Bruker) were performed (Tab. 2). It is observed that the real concentration Eu^{3+} cation is very close to the nominal one, confirming the replacement of Ca^{2+} by Eu^{3+} cations.

Table 2. Crystallite size (D) and lattice strain (ε) obtained by Scherrer's equation and Williamson-Hall model, and Eu concentration obtained by XRF analysis.

Sample	Scherrer		Williamson-Hall		[Eu] (%)	
	D (nm)	ε (10^{-3})	D (nm)	ε (10^{-3})	Nominal	Real
CZ	31.72	16.98	24.30	18.82	0.0000	0.0000
CZE1	31.58	13.81	20.91	32.53	0.0010	0.0008
CZE2	31.64	30.76	23.76	30.09	0.0020	0.0018
CZE4	31.68	34.93	31.48	16.44	0.0040	0.0041
CZE8	31.42	56.64	17.98	34.07	0.0080	0.0077

The band gap energy (E_{gap}) value was obtained through the Kulbelka-Munk (Yang and Kruse, 2004) calculation for CZ and CZE samples. The E_{gap} values of the samples were 5.75, 5.66, 5.62, 5.60, and 5.35 eV for the samples CZ, CZE1, CZE2, CZE4, and CZE8, respectively. The E_{gap} value obtained for the CZ sample is close to the value obtained in previous works (Maurya *et al.*, 2016; Yamaguchi *et al.*, 2000; Zeba *et al.*, 2020). This decrease occurs because the incorporation of Eu^{3+} cations in the CZ structure causes new defects and intermediate levels close to the valence (VB) and conduction (CB) bands, which leads to a decrease in E_{gap} (Cyriac *et al.*, 2018; Gupta *et al.*, 2015a).

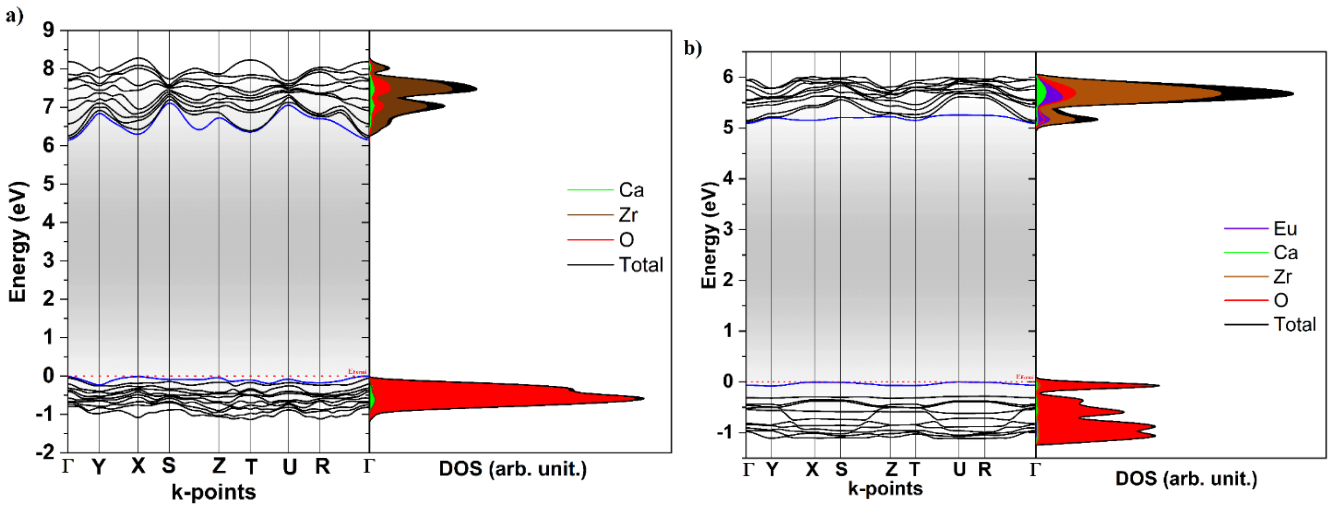

Figure 3. Band structure and DOS profiles for **(a)** CZ, and **(b)** CZE materials.

The calculated band structure and density of states (DOS) projected for the atoms and orbitals of CZ and CZE models are displayed in Fig. 3. An analysis of the band structure and projected DOS presented here reveals that the direct transition is produced along the k-points Γ-Γ (000 to 000) and U-Γ (101 to 000) from the top of the VB to the bottom of the CB of pure and doped models, respectively. The E_{gap} values is 6.23 eV to CZ and 5.09 eV to CZE 12.5% model. As regard the

Eclética Química Journal, vol. 47, special issue 1, 2022, 90-104
ISSN: 1678-4618
DOI: 10.26850/1678-4618eqj.v47.1SI.2022.p90-104

obtained E_{gap} values, experimental and theoretical values were compared evidencing a good agreement.

An analysis of the DOS, the main contribution to the valence band maximum (VBM) region is due to the 2*p* (p_x, p_y, and p_z), orbitals from the O atoms and a predominance of the 4*d* (d_z^2, $d_{x^2-y^2}$, d_{xy}, d_{xz}, d_{yz}) and 4*f* (f^3, f_{xz^2}, f_{yz^2}, $f_{z(x^2-y^2)}$, f_{xyz}, $f_{x(x^2-3y^2)}$, $f_{y(3x^2-y^2)}$) states formed by Zr and Eu atoms is found in the conduction band minimum (CBM) region, situated from 6.23 to 9 eV (CZ) and from 5.09 to 6.5 eV (CZE 12.5%) and with a small contribution from Ca orbitals.

Additionally, the Fig. 4 summarizes the electronic density maps of the CZ and CZE (12.5%) models obtained from the optimized wavefunction, where the electronic density matrix was resolved as isolines that describe the density in an area. These electronic density maps were described along the Ca−O, Zr−O, and Eu−O bonds direction of the models, which corresponds more specifically to the diagonal (110) plane (Fig. 4).

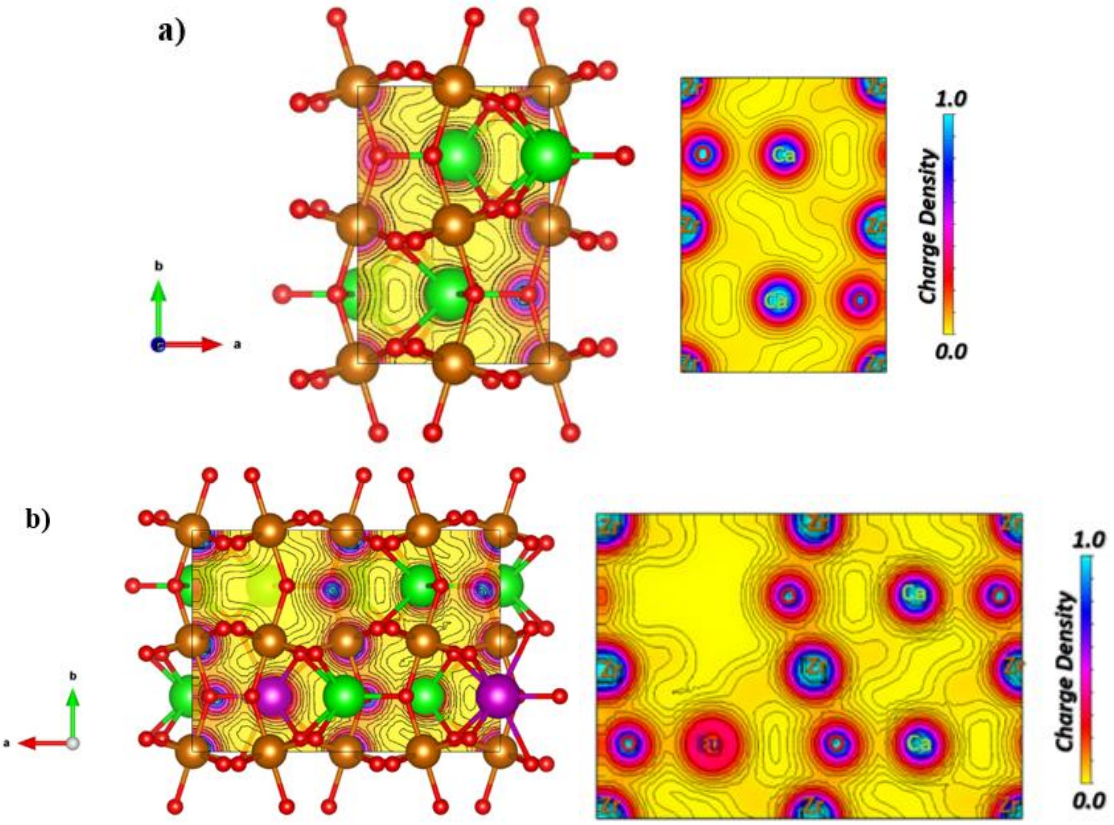

Figure 4. Electron density maps in the diagonal plane (110) for **(a)** CZ, and **(b)** CZE materials.

To observe the possible application of CZE samples as a red emitter, the samples were first excited with a laser at 325 nm (Fig. 5). The CZ sample has a broadband emission profile, characteristic of a multiphonic process, involving several intermediate energy states (Gupta *et al*., 2015b). The maximum emission of the CZ sample is found in approximately 447 nm, in the blue region, which is the result of internal charge transfers of O 2*p* to Zr 4*d* orbitals (Oliveira *et al*., 2017). For CZE samples, the broadband emission characteristic of the CZ sample is no longer observed, giving space to the specific emission of Eu^{3+} cations. The characteristic emission bands of the Eu^{3+} cations are located at 584, 596, 615, 659, and 705 nm can be assigned to the transitions $^5D_0 \rightarrow {}^7F_J$, J = 0, 1, 2, 3, and 4, respectively (D'Achille *et al*., 2021; Gnanam *et al*., 2021; M. Liu *et al*., 2021; Riul *et al*. 2021). The intensity of the CZE samples is proportional to the concentration of Eu^{3+} cations, being the CZE1 sample the least intense and CZE8 sample the most intense. The maximum emission of CZE samples was attributed to the $^5D_0 \rightarrow {}^7F_2$ transitions (615 nm). The appearance of these transitions confirms the CZ structure as a good host matrix for sensitizing the red emission of Eu^{3+} cations.

Eclética Química Journal, vol. 47, special issue 1, 2022, 90-104
ISSN: 1678-4618
DOI: 10.26850/1678-4618eqj.v47.1SI.2022.p90-104

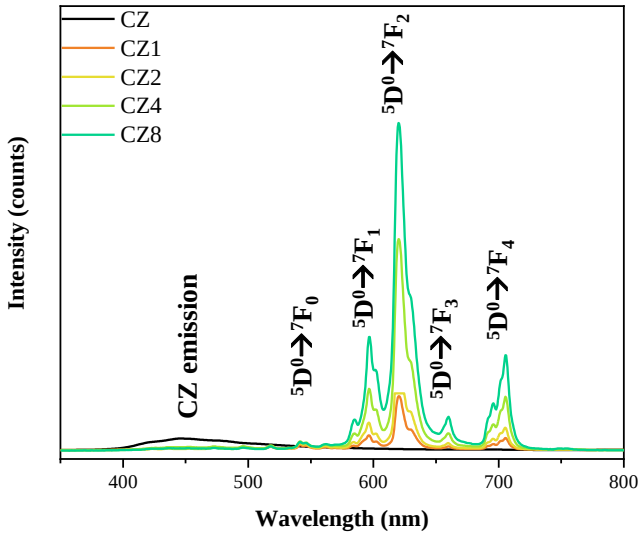

Figure 5. Emission spectra of CZ, and CZE materials excited at 325 nm.

Figure 6a shows the excitation spectra of CZE samples under 614 nm emission band. At 280 nm a broad band related to the CZ matrix is observed. According to Dorenbos (2003), this emission related to the charge transfer band (CTB) of O^{2-} to Eu^{3+}. It is also observed the emissions referring to the transitions of the Eu^{3+} cations for CZE samples. These transitions are $^7D_0 \rightarrow {}^5D_J$ (J = 2, 3 and 4), $^7F_0 \rightarrow {}^5L_J$ (J = 6, 7 and 8) and $^7F_0 \rightarrow {}^5G_J$ (J = 4, 5 and 6) (Vieira *et al.*, 2019). The most intense is located at 394 nm referring to the $^7F_0 \rightarrow {}^5L_6$ transition. This transition in specific is useful for applications in near-UV and LEDs (Hou *et al.*, 2012; Singh *et al.*, 2021). The emission spectra of CZE samples excited at 394 nm was shown in Fig. 6b. It is observed that the transitions $^5D_0 \rightarrow {}^7F_J$, J = 0, 1, 2, 3, and 4, become more defined, locating at 565, 592, 616, 655, and 703 nm (Chen *et al.*, 2000; X. Liu *et al.*, 2007; Song *et al.*, 2010). The red emission at 616 nm is due to the $^5D_0 \rightarrow {}^7F_2$ electric-dipole transition that is parity forbidden and hypersensitive by the crystalline field (Baig *et al.*, 2021; Bharathi *et al.*, 2021; Wu *et al.*, 2021). The $^5D_0 \rightarrow {}^7F_1$ magnetic-dipole transition is located at 592 nm it is not affected by the environment (Kalu *et al.*, 2021; Lakde *et al.*, 2021; Peipei *et al.*, 2021). So, the integrated area ratio of the peaks corresponding to $^5D_0 \rightarrow {}^7F_2$ and $^5D_0 \rightarrow {}^7F_1$ transitions provides information on the changes in the environment around the Eu^{3+} cations (Parchur and Ningthoujam, 2012). The values obtained for the samples are 4.92, 4.91, 4.81, and 4.66 for the samples CZE1, CZE2, CZE4, and CZE8. These values are very close and indicate that the Eu^{3+} environment changes to a higher symmetry site with the increase in the concentration of Eu^{3+} cations, since the ratio of the relative areas decreases with the increase of the Eu-doping. (P. Almeida *et al.*, 2021; Mazzo *et al.*, 2010; Pinatti *et al.*, 2015).

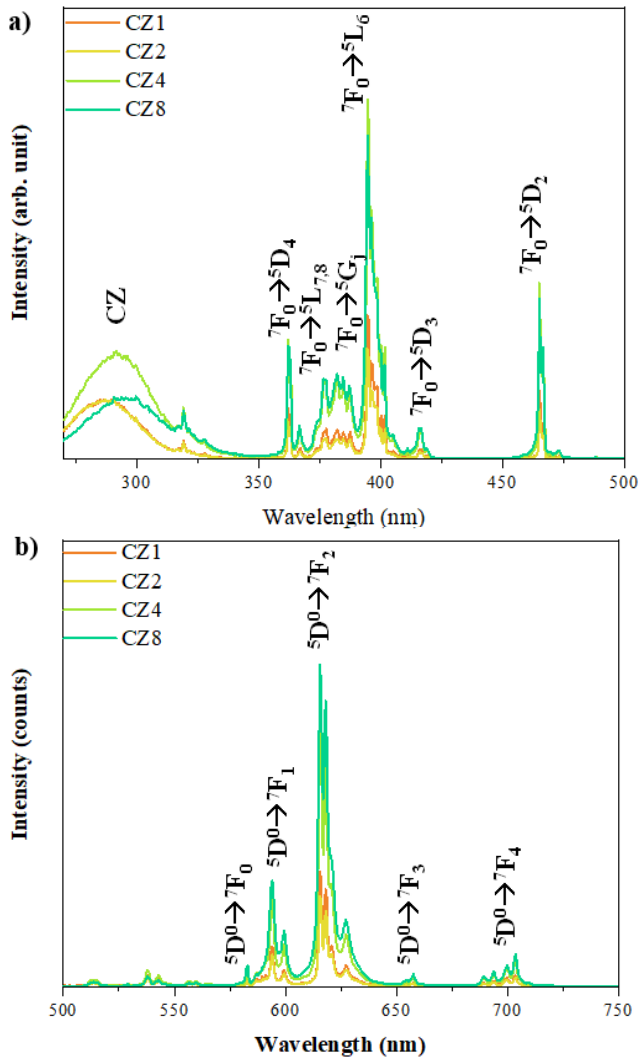

Figure 6. **(a)** Excitation and **(b)** emission spectrum of CZE samples monitoring the emission at 614 nm and excited at 394 nm, respectively.

Figure 7a depicts the decay behavior of the $^5D_0 \rightarrow {}^7F_2$ transition for Eu^{3+} cations in the CZE samples, using the emission and excitation wavelengths fixed at 614 and 394 nm, respectively (He *et al.*, 2018; Parchur *et al.*, 2011). These life times were fitted using a monoexponential function (Eq. 5):

$$y = y_0 + A_1 exp\left(\frac{t}{\tau}\right) \quad (5)$$

where y is the intensity; y_0 is the intensity at the 0 ms; A_1 is the amplitude and τ is the lifetime of the $^5D_0 \rightarrow {}^7F_2$ transition (Nyein *et al.*, 2003).

Eclética Química Journal, vol. 47, special issue 1, 2022, 90-104
ISSN: 1678-4618
DOI: 10.26850/1678-4618eqj.v47.1SI.2022.p90-104

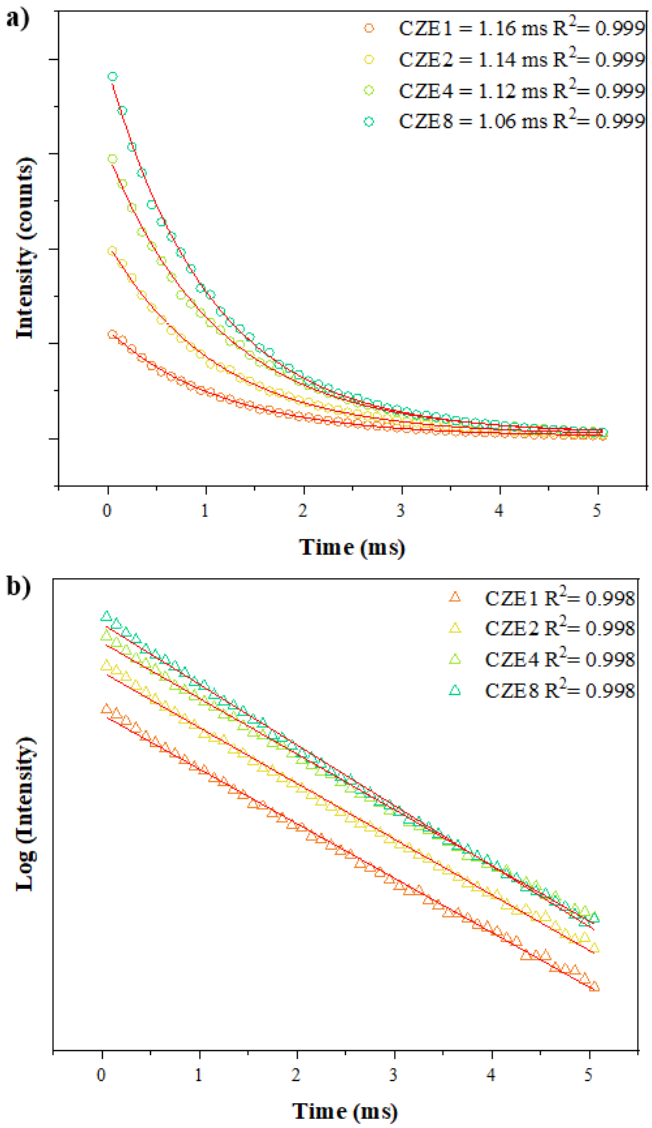

Figure 7. **(a)** Decay curves and **(b)** Log of the decay curves $^5D_0 \rightarrow {}^7F_2$ transition of CZE samples.

Excited state τ values determined were 1.16, 1.14, 1.12, and 1.06 ms to CZE1, CZE2, CZE4, and CZE8, respectively. The excited state τ values of Eu^{3+} cations decreased with increasing doping concentration due the exchange interactions between activated ions pairs and the higher concentration of the activated ions density around quenching center. Figure 7b shows the monoexponential decay of the samples fitted with an exponential function as the Eq. 5. The energy transfer rate between Eu^{3+}–Eu^{3+} (η_{Eu-Eu}) was calculated by the Eq. 6:

$$\eta_{Eu-Eu} = 1 - \frac{\tau_{CZE}}{\tau_{CZEH}} \quad (6)$$

where τ_{CZE} is the lifetime of CZE samples and τ_{CZEH} is the lifetime of the sample with higher τ (in this case, 1.16 ms to CZE1) (Kunti *et al.*, 2021).

The obtained η_{Eu-Eu} values were 1.72, 3.44 and 8.62, for CZE2, CZE4 and CZE8, respectively. The distance between Eu^{3+} cations decrease with increasing concentration of these cations in the CZ host matrix, causing an energy transfer more efficient and allowing new decay channels (Kunti *et al.*, 2021). These extra channels provide new radiative and nonradiative transition probabilities decreasing the lifetime (İlhan and Keskin, 2018). The efficiency of energy transfer (η_{ET}) (Eq. 7):

$$\eta_{ET} = 1 - \frac{\tau_{CZE}}{\tau_{CZ}} \quad (7)$$

where τ_{CZE} is the lifetime of CZE samples and τ_{CZ} is the lifetime of the CZ sample (2.57 in this case) (Li *et al.*, 2007).

The obtained η_{ET} values were 0.5486, 0.5564, 0.5642, and 0.5875 for the CZE1, CZE2, CZE4, and CZE8, respectively. As expected, the energy transfer efficiency (η_{ET}) goes hand in hand with the increase in the concentration of Eu^{3+} cations.

Figure 8 shows the color variations of the characteristic emissions of the samples according to the Commission Internationale de L'Éclairage (CIE) (Du *et al.*, 2013). As a characteristic emission, for the CZ sample its emission in blue region is observed at 325 and yellow at 394 nm. However, for the CZE samples, with the increase in the amount of Eu^{3+} cations in the CZ host matrix, a displacement towards the red region is observed, reaching almost pure red emission in both excitations.

In addition, theoretical methodology can contribute to an explanation for the optical properties, since a reduction in the band gap value and the PL emissions of CZ and CZE models. In order to clarify the effect of Eu^{3+} cations on the PL emissions of CZ, it was proposed a general scheme combining the DOS and band structure calculations for CZ and CZE models, as shown in Fig. 9.

Eclética Química Journal, vol. 47, special issue 1, 2022, 90-104
ISSN: 1678-4618
DOI: 10.26850/1678-4618eqj.v47.1SI.2022.p90-104

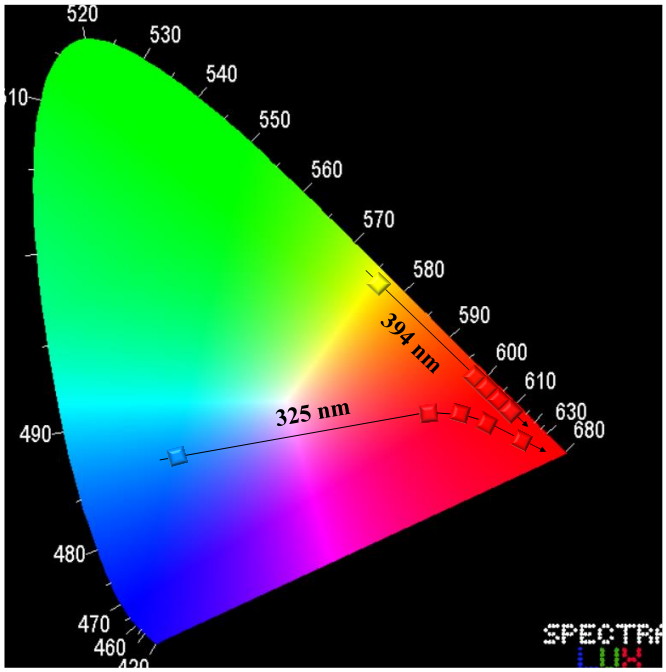

Figure 8. CIE coordinates of CZ and CZE samples excited at 325 and 394 nm.

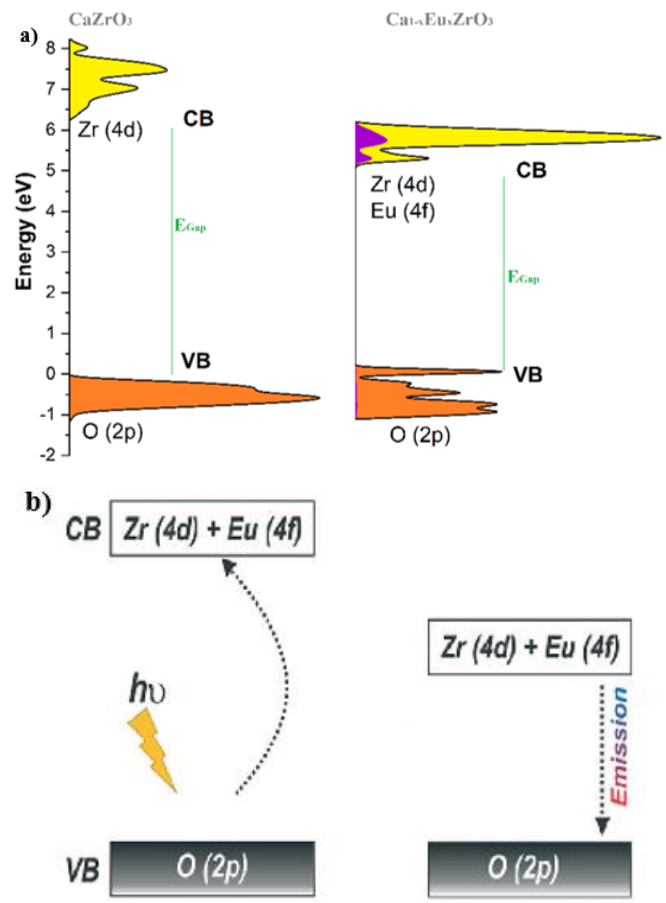

Figure 9. Scheme representing **(a)** the electronic structure for pure CZ and CZE materials; **(b)** photoinduced electron transfer mechanism from the VB to the CB to light emission.

Doping with Eu^{3+} cations generate a new electron density distribution, being located on the oxygen-mediated $[EuO_8]$–$[ZrO_6]$ interaction, to which is trapped in empty Zr (4*d*) and Eu (4*f*) orbitals. Initially, the Eu^{3+} cations doping process induces the formation of V_{Ca} sites that perturb the VB energy levels and promotes the insertion of 4*f* orbitals in the CBM; in other words, intermediate energy levels are introduced in the E_{gap} region, reducing the energy required for electron transfer (Fig. 9a). The next step is the photoinduced electron transfer from the VB to the CB, generating an electron–hole pair within the CZE electronic structure (Fig. 9b). This step is crucial because it offers a new interpretation of the optical properties of a material.

In addition, a deeper insight into the PL emission of pure and Eu-doped structures, based on the effective mass of electrons (m_e*) and holes (m_h*), following the procedure reported in a previous study is presented in Tab. 3 (Silva *et al.*, 2020). Such an approach is effective in discussing the photoinduced properties of solid-state materials once the effective mass allows one to ascertain the mobility of the charge carriers.

Table 3. Calculated effective mass of electrons (me*) and holes (mh*) of CZ and CZE 12.5%.

Effective mass of electrons and holes CZ		
m_e*	m_h*	m_e*/ m_h*
0.31	2.46	0.126
Effective mass of electrons and holes CZE		
m_e*	m_h*	m_e*/ m_h*
0.49	0.94	0.516

The calculated values reported in Tab. 3 for CZ and CZE indicates that excited electrons are lighter than generated holes. Also, it was observed that Eu-doping induces a heavier (lighter) electron (hole) effective mass in comparison to CZ, increasing the hole mobility that contributes to increase the electron–hole recombination rate, explaining the superior PL properties of CZE. This fact can be associated with the bonding character of Eu−O interactions in comparison to Ca−O summed to the presence of V_{Ca} in the doped crystalline structure due to the electron density redistribution that governs the band gap narrowing for doped samples, as confirmed in Fig. 9. Once the Eu−O bonds are more covalent than Ca−O, the band curvature is affected, and the effective mass of electrons and holes is controlled from doping.

Eclética Química Journal, vol. 47, special issue 1, 2022, 90-104
ISSN: 1678-4618
DOI: 10.26850/1678-4618eqj.v47.1SI.2022.p90-104

4. Conclusions

In this paper, a simple sol-gel method followed by a soft thermal treatment without any surfactant was applied to investigate the influence of Eu^{3+} cations in the host matrix of CZ. The $Ca_{1-x}ZrO_3$:Eu_x crystals (x = 0.01, 0.02, 0.04, and 0.08 mol%) were characterized by XRD and the patterns confirms that the Eu-doped samples present an orthorhombic structure as the CZ pure. However, the results shows that the replacement of Ca^{2+} by Eu^{3+} cations induce local defects in the lattice causing distortions in the [CaO_8], [ZrO_6], and [EuO_8] clusters, as well as changes in the lattice parameters and an expansion of cell parameters. The micro-Raman results disclosure that the presence of Eu^{3+} cations in the host matrix of CZ caused a loss of definition in the modes located at 177, 184, 205, 221, and 229 cm^{-1} due to the increase in local disorder. The real amount of Eu^{3+} cations in the CZE samples was verified by XRF and the results confirms the presence of Eu^{3+} cations in the host matrix. The substitution of Ca^{2+} by Eu^{3+} cations also affected the E_{gap} value in which a decrease with the increase of Eu^{3+} cations amount in the host matrix was observed, and this result was endorsed by the first-principles calculations. According to the DOS analysis, the electronic density in the VBM is due to the O 2*p* orbitals and a predominance of the Zr 4*d* and Eu 4*f* orbitals is observed in the CBM. The luminescence profile of the sample was investigated, and the results show that the intensity of the CZE samples is proportional to the concentration of Eu^{3+} cations, being the CZE1 sample the least intense and CZE8 the most intense. The appearance of the $^5D_0 \rightarrow {}^7F_2$ transitions (615 nm) confirms that the $CaZrO_3$ structure is a good host matrix for sensitizing the red emission of Eu^{3+} cations. From the experimental and theoretical results, it was proposed a general luminescence scheme for the CZE samples.

Authors' contribution

Conceptualization: Assis, M.; Oliveira, M. C.; Gouveia, A. F.; Ribeiro, R. A. P.
Data curation: Assis, M.; Ribeiro, R. A. P.; Bort, J. M. A.; Longo, E.
Formal Analysis: Assis, M.; Oliveira, M. C.; Gouveia, A. F.; Ribeiro, L. K.; Ribeiro, R. A. P.
Funding acquisition: Rosa, I. L. V.; Ribeiro, R. A. P.; Bort, J. M. A.; Longo, E.
Investigation: Assis, M.; Oliveira, M. C.; Gouveia, A. F.; Ribeiro, L. K.; Ribeiro, R. A. P.
Methodology: Assis, M.; Oliveira, M. C.
Project administration: Bort, J. M. A.; Longo, E.
Resources: Rosa, I. L. V.; Ribeiro, R. A. P.; Bort, J. M. A.; Longo, E.
Software: Oliveira, M. C.; Gouveia, A. F.; Ribeiro, R. A. P.; Bort, J. M. A.
Supervision: Rosa, I. L. V.; Ribeiro, R. A. P.; Bort, J. M. A.; Longo, E.
Validation: Assis, M.; Oliveira, M. C.; Gouveia, A. F.; Ribeiro, R. A. P.
Visualization: Assis, M.; Oliveira, M. C.; Gouveia, A. F.; Ribeiro, R. A. P.
Writing – original draft: Assis, M.; Oliveira, M. C.; Gouveia, A. F.; Ribeiro, L. K.; Ribeiro, R. A. P.
Writing – review & editing: Assis, M.; Oliveira, M. C.; Gouveia, A. F.; Ribeiro, L. K.; Ribeiro, R. A. P.

Data availability statement

The data will be available upon request.

Funding

Fundação de Amparo à Pesquisa do Estado de São Paulo (FAPESP). Grant No: 2013/07296-2; 2019/01732-1.

Universitat Jaume I. Project: UJI-B2019-30.

Acknowledgments

The authors acknowledge the support of institutes: CDMF (Centro de Desenvolvimento de Materiais Funcionais), Universidade Federal de São Carlos/FAPESP and Universitat Jaume I. M.A. was supported by the Margarita Salas postdoctoral contract MGS/2021/21(UP2021-021) financed by the European Union-NextGenerationEU. J.A. acknowledges Universitat Jaume I (project UJI-B2019-30), the Generalitat Valenciana (Project AICO/2020/329), and the Ministerio de Ciencia, Innovación y Universidades (Spain) (project PGC2018094417-B-I00) for financially supporting this research. A.F.G acknowledges the Universitat Jaume I for the postdoctoral contract (POSDOC/2019/30).

References

Al Boukhari, J.; Khalaf, A.; Hassan, R. S.; Awad, R. Structural, optical and magnetic properties of pure and rare earth-doped NiO nanoparticles. *Appl. Phys. A* **2020**, *126*, 323. https://doi.org/10.1007/s00339-020-03508-3

Almeida, P. B.; Pinatti, I. M.; de Oliveira, R. C.; Teixeira, M. M.; Santos, C. C.; Machado, T. R.; Longo, E.; Rosa, I. L. V.

Structural, morphological and photoluminescence properties of β-Ag_2MoO_4 doped with Eu^{3+}. *Chem. Pap.* **2021**, *75*, 1869–1882. https://doi/10.1007/s11696-020-01489-4

Almeida, T. H.; Almeida, D. H.; Gonçalves, D.; Lahr, F. A. R. Color variations in CIELAB coordinates for softwoods and hardwoods under the influence of artificial and natural weathering. *J. Build. Eng.* **2021**, *35* (3), 101965. https://doi.org/10.1016/j.jobe.2020.101965

André, R. S.; Zanetti, S. M.; Varela, J. A.; Longo, E. Synthesis by a chemical method and characterization of $CaZrO_3$ powders: Potential application as humidity sensors. *Ceram. Int.* **2014**, *40* (10) (Part B), 16627–16634. https://doi.org/10.1016/j.ceramint.2014.08.023

Bai, J.-M.; Zhang, L.; Liang, R.-P.; Qiu, J.-D. Graphene Quantum Dots Combined with Europium Ions as Photoluminescent Probes for Phosphate Sensing. *Chem. – A Eur. J.* **2013**, *19* (12), 3822–3826. https://doi.org/10.1002/chem.201204295

Baig, N.; Kadam, A. R.; Dubey, K.; Dhoble, N. S.; Dhoble, S. J. Wet chemically synthesized $Na_3Ca_2(SO_4)_3Cl:RE^{3+}$ (RE= Ce, Dy, Eu) phosphors for solid-state lighting. *Radiat. Eff. Defects Solids* **2021**, *176* (5–6), 493–507. https://doi.org/10.1080/10420150.2021.1871735

Becke, A. D. Density-functional thermochemistry. III. The role of exact exchange. *J. Chem. Phys.* **1993**, *98*, 5648. https://doi.org/10.1063/1.464913

Bharathi, N. V.; Jeyakumaran, T.; Ramaswamy, S.; Jayabalakrishnan, S. S. Synthesis and characterization of a Eu^{3+}-activated $Ba_{2-x}V_2O_7:xEu^{3+}$ phosphor using a hydrothermal method: a potential material for near-UV-WLED applications. *Luminescence* **2021**, *36* (4), 849–859. https://doi.org/10.1002/bio.4031

Chen, W.; Malm, J.-O.; Zwiller, V.; Huang, Y.; Liu, S.; Wallenberg, R.; Bovin, J.-O.; Samuelson, L. Energy structure and fluorescence of Eu^{2+} in ZnS:Eu nanoparticles. *Phys. Rev. B* **2000**, *61*, 11021. https://doi.org/10.1103/PhysRevB.61.11021

Chu, H.; Yao, D.; Chen, J.; Yu, M.; Su, L. Double-Emission Ratiometric Fluorescent Sensors Composed of Rare-Earth-Doped ZnS Quantum Dots for Hg^{2+} Detection. *ACS Omega* **2020**, *5* (16), 9558–9565. https://doi.org/10.1021/acsomega.0c00861

Cyriac, J.; Mathew, S.; Augustine, S.; Nambissan, P. M. G. Defects characterization studies of europium-substituted bismuth ferrite nanocrystals by positron annihilation and other methods. *J. Phys. D. Appl. Phys.* **2018**, *51* (43), 435303. https://doi.org/10.1088/1361-6463/aadfa7

D'Achille, A. E.; Wallace, R. M.; Coffer, J. L. Morphology-dependent fluorescence of europium-doped cerium oxide nanomaterials. *Nanoscale Adv.* **2021**, *3* (12), 3563–3572. https://doi.org/10.1039/D1NA00096A

De La Pierre, M.; Carteret, C.; Maschio, L.; André, E.; Orlando, R.; Dovesi, R. The Raman spectrum of $CaCO_3$ polymorphs calcite and aragonite: A combined experimental and computational study. *J. Chem. Phys.* **2014**, *140* (16), 164509. https://doi.org/10.1063/1.4871900

Dorenbos, P. Systematic behaviour in trivalent lanthanide charge transfer energies. *J. Phys Condens. Matter* **2003**, *15* (49), 8417. https://doi.org/10.1088/0953-8984/15/49/018

Dovesi, R.; Erba, A.; Orlando, R.; Zicovich-Wilson, C. M.; Civalleri, B.; Maschio, L.; Rérat, M.; Casassa, S.; Baima, J.; Salustro, S.; Kirtman, B. Quantum-mechanical condensed matter simulations with CRYSTAL. *Wiley Interdiscip. Rev. Comput. Mol. Sci.* **2018**, *8* (4), e1360. https://doi.org/10.1002/wcms.1360

Du, Q.; Zhou, G.; Zhou, J.; Zhou, H. Combustion synthesis and photoluminescence properties of $CaZrO_3:Eu^{3+}$ with highly enhanced brightness by Li^+ doping. *J. Lumin.* **2013**, *137*, 83–87. https://doi.org/10.1016/j.jlumin.2012.12.046

Dubey, V.; Tiwari, N. Structural and optical analysis on europium doped $AZrO_3$ (A=Ba, Ca, Sr) phosphor for display devices application. *AIP Conf. Proc.* **2016**, *1728*, 020002. https://doi.org/10.1063/1.4946052

Eglitis, R. I.; Purans, J.; Gabrusenoks, J.; Popov, A. I.; Jia, R. Comparative Ab Initio Calculations of ReO_3, $SrZrO_3$, $BaZrO_3$, $PbZrO_3$ and $CaZrO_3$ (001) Surfaces. *Crystals* **2020**, *10* (9), 745. https://doi.org/10.3390/cryst10090745

El-Bahy, Z. M.; Ismail, A. A.; Mohamed, R. M. Enhancement of titania by doping rare earth for photodegradation of organic dye (Direct Blue). *J. Hazard. Mater.* **2009**, *166* (1), 138–143. https://doi.org/10.1016/j.jhazmat.2008.11.022

Evangeline, B.; Azeem, P. A.; Prasada Rao, R.; Swati, G.; Haranath, D. Structural and luminescent features of cerium doped $CaZrO_3$ blue nanophosphors. *J. Alloys Compd.* **2017**, *705*, 618–623 https://doi.org/10.1016/j.jallcom.2016.11.115

Fernandes, S. L.; Gasparotto, G.; Teixeira, G. F.; Cebim, M. A.; Longo, E.; Zaghete, M. A. Lithium lanthanum titanate perovskite ionic conductor: Influence of europium doping on structural and optical properties. *Ceram. Int.* **2018**, *44* (17), 21578–21584. https://doi.org/10.1016/j.ceramint.2018.08.221

Fukushima, H.; Nakauchi, D.; Kato, T.; Kawaguchi, N.; Yanagida, T. Scintillation and luminescence properties of undoped and europium-doped $CaZrO_3$ crystals. *J. Lumin.* **2020**, *223*, 117231. https://doi.org/10.1016/j.jlumin.2020.117231

Gnanam, S.; Gajendiran, J.; Ramya, J. R.; Ramachandran, K.;

Raj, S. G. Glycine-assisted hydrothermal synthesis of pure and europium doped CeO_2 nanoparticles and their structural, optical, photoluminescence, photocatalytic and antibacterial properties. *Chem. Phys. Lett.* **2021**, *763*, 138217. https://doi.org/10.1016/j.cplett.2020.138217

Gupta, S. K.; Ghosh, P. S.; Sudarshan, K.; Gupta, R.; Pujari, P. K.; Kadam, R. M. Multifunctional pure and Eu^{3+} doped β-Ag_2MoO_4: photoluminescence, energy transfer dynamics and defect induced properties. *Dalton Trans.* **2015a**, *44* (44), 19097–19110. https://doi.org/10.1039/C5DT03113C

Gupta, S. K.; Ghosh, P. S.; Pathak, N.; Tewari, R. Nature of defects in blue light emitting $CaZrO_3$: Spectroscopic and theoretical study. *RSC Adv.* **2015b**, *5* (70), 56526–56533. https://doi.org/10.1039/C5RA09637E

He, C.; Ji, H.; Huang, Z.; Zhang, X.; Liu, H.; Liu, S.; Liu, Y.; Fang, M.; Wu, X.; Min, X. Preparation and photoluminescence properties of red-emitting phosphor $ZnAl_2O_4$:Eu^{3+} with an intense $^5D_0 \rightarrow {}^7F_0$ transition. *Mater. Res. Express* **2018**, *5* (2), 025501. https://doi.org/10.1088/2053-1591/aaa7c9

Holzapfel, N. P.; Majher, J. D.; Strom, T. A.; Moore, C. E.; Woodward, P. M. $Cs_4Cd_{1-x}Mn_xBi_2Cl_{12}$—A Vacancy-Ordered Halide Perovskite Phosphor with High-Efficiency Orange-Red Emission. *Chem. Mater.* **2020**, *32* (8), 3510–3516. https://doi.org/10.1021/acs.chemmater.0c00454

Hou, J.; Yin, X.; Fang, Y.; Huang, F.; Jiang, W. Novel red-emitting perovskite-type phosphor $CaLa_{1-x}MgM'O6$: xEu^{3+} (M′=Nb, Ta) for white LED application. *Opt. Mater.* **2012**, *34* (8), 1394–1397. https://doi.org/10.1016/j.optmat.2012.02.031

İlhan, M.; Keskin, İ. Ç. Photoluminescence, radioluminescence and thermoluminescence properties of Eu^{3+} doped cadmium tantalate phosphor. *Dalton Trans.* **2018**, *47* (39), 13939–13948. https://doi.org/10.1039/C8DT02395F

Jayachandraiah, C.; Kumar, K. S.; Krishnaiah, G.; Rao, N. M. Influence of Dy dopant on structural and photoluminescence of Dy-doped ZnO nanoparticles. *J. Alloys Compd.* **2015**, *623*, 248–254. https://doi.org/10.1016/j.jallcom.2014.10.067

Kalu, O.; Ahemen, I.; Esparza Ponce, H. E.; Moller, J. A. D.; Reyes-Rojas, A. Red-emission analysis, Judd–Ofelt intensity parameters and laser properties of CdMgZnO:xEu^{3+} nanocrystals: the effects of Eu^{3+} concentration. *J. Phys. D. Appl. Phys.* **2021**, *54*, 345108. https://doi.org/10.1088/1361-6463/ac021c

Katyayan, S.; Agrawal, S. Synthesis and Investigation of Structural and Optical Properties of Eu^{3+} Doped $CaZrO_3$ Phosphor. *Mater. Today Proc.* **2017**, *4* (8), 8016–8024. https://doi.org/10.1016/j.matpr.2017.07.139

Khan, A.; Song, F.; Zhou, A.; Gao, X.; Feng, M.; Ikram, M.; Hu, H.; Sang, X.; Liu, L. Tuning white light upconversion emission from $Yb^{3+}/Er^{3+}/Tm^{3+}$ triply doped $CaZrO_3$ by altering Tm^{3+} concentration and excitation power. *J. Alloys Compd.* **2020**, *835*, 155286. https://doi.org/10.1016/j.jallcom.2020.155286

Khan, A.; Song, F.; Gao, X.; Chen, Z.; Sang, X.; Feng, M.; Liu, L. Introduction of Molybdenum into the lattice of single-host $CaZrO_3$: Dy^{3+}/Eu^{3+} to enhance luminescence intensity of the phosphor for white light emission. *J. Alloys Compd.* **2021**, *881*, 160652. https://doi.org/10.1016/j.jallcom.2021.160652

Kumar, S. G. P.; Krishna, R. H.; Kottam, N.; Murthy, P. K.; Manjunatha, C.; Preetham, R.; Shivakumara, C.; Thomas, T. Understanding the photoluminescence behaviour in nano $CaZrO_3$:Eu^{3+} pigments by Judd-Ofelt intensity parameters. *Dyes Pigm.* **2018**, *150*, 306–314. https://doi.org/10.1016/j.dyepig.2017.12.022

Kumar P. R.; Prasad, N.; Veillon, F.; Prellier, W. Raman spectroscopic and magnetic properties of Europium doped nickel oxide nanoparticles prepared by microwave-assisted hydrothermal method. *J. Alloys Compd.* **2021**, *858*, 157639. https://doi.org/10.1016/j.jallcom.2020.157639

Kunti, A. K.; Patra, N.; Harris, R. A.; Sharma, S. K.; Bhattacharyya, D.; Jha, S. N.; Swart, H. C. Structural properties and luminescence dynamics of $CaZrO_3$:Eu^{3+} phosphors. *Inorg. Chem. Front.* **2021**, *8* (3), 821–836. https://doi.org/10.1039/D0QI01178A

Lahtinen, S.; Wang, Q.; Soukka, T. Long-Lifetime Luminescent Europium(III) Complex as an Acceptor in an Upconversion Resonance Energy Transfer Based Homogeneous Assay. *Anal. Chem.* **2016**, *88* (1), 653–658. https://doi.org/10.1021/acs.analchem.5b02228

Lakde, J.; Mehare, C. M.; Pandey, K. K.; Dhoble, N. S.; Dhoble, S. J. Recent development of Eu^{3+}-doped phosphor for white LED application: A review. *J. Phys. Conf. Ser.* **2021**, *1913*, 012029. https://doi.org/10.1088/1742-6596/1913/1/012029

Lee, C.; Yang, W.; Parr, R.G. Development of the Colle-Salvetti correlation-energy formula into a functional of the electron density. *Phys. Rev. B* **1988**, *37*, 785. https://doi.org/10.1103/PhysRevB.37.785

Levin, I.; Amos, T. G.; Bell, S. M.; Farber, L.; Vanderah, T. A.; Roth, R. S.; Toby, B. H. Phase equilibria, crystal structures, and dielectric anomaly in the $BaZrO_3$–$CaZrO_3$ system. *J. Solid State Chem.* **2003**, *175* (2), 170–181. https://doi.org/10.1016/S0022-4596(03)00220-2

Li, Y.-C.; Chang, Y.-H.; Chang, Y.-S.; Lin, Y.-J.; Laing, C.-H. Luminescence and Energy Transfer Properties of Gd^{3+} and Tb^{3+} in $LaAlGe_2O_7$. *J. Phys. Chem. C* **2007**, *111* (28), 10682–10688. https://doi.org/10.1021/jp0719107

Liu, X.; Lin, C.; Lin, J. White light emission from Eu^{3+} in $CaIn_2O_4$ host lattices. *Appl. Phys. Lett.* **2007**, *90*, 081904. https://doi.org/10.1063/1.2539632

Liu, W.; Zhang, H.; Wang, H.-g.; Zhang, M.; Guo, M. Titanium mesh supported TiO_2 nanowire arrays/upconversion luminescence Er^{3+}-Yb^{3+} codoped TiO_2 nanoparticles novel composites for flexible dye-sensitized solar cells. *Appl. Surf. Sci.* **2017**, *422*, 304–315. https://doi.org/10.1016/j.apsusc.2017.06.007

Liu, M.; Shu, M.; Yan, J.; Liu, X.; Wang, R.; Hou, Z.; Lin, J. Luminescent net-like inorganic scaffolds with europium-doped hydroxyapatite for enhanced bone reconstruction. *Nanoscale* **2021**, *13* (2), 1181–1194. https://doi.org/10.1039/D0NR05608A

Lovisa, L. X.; Araújo, V. D.; Tranquilin, R. L.; Longo, E.; Li, M. S.; Paskocimas, C. A.; Bomio, M. R. D.; Motta, F. V. White photoluminescence emission from ZrO_2 co-doped with Eu^{3+}, Tb^{3+} and Tm^{3+}. *J. Alloys Compd.* **2016**, *674*, 245–251. https://doi.org/10.1016/j.jallcom.2016.03.037

Manohar, A.; Krishnamoorthi, C.; Pavithra, C.; Thota, N. Magnetic Hyperthermia and Photocatalytic Properties of $MnFe_2O_4$ Nanoparticles Synthesized by Solvothermal Reflux Method. *J. Supercond. Nov. Magn.* **2021**, *34*, 251–259. https://doi.org/10.1007/s10948-020-05685-x

Maurya, A.; Yadav, R. S.; Yadav, R. V; Rai, S. B.; Bahadur, A. Enhanced green upconversion photoluminescence from Ho^{3+}/Yb^{3+} co-doped $CaZrO_3$ phosphor via Mg^{2+} doping. *RSC Adv.* **2016**, *6* (114), 113469–113477. https://doi.org/10.1039/C6RA23835A

Mazzo, T. M.; Moreira, M. L.; Pinatti, I. M.; Picon, F. C.; Leite, E. R.; Rosa, I. L. V; Varela, J. A.; Perazolli, L. A.; Longo, E. $CaTiO_3$:Eu^{3+} obtained by microwave assisted hydrothermal method: A photoluminescent approach. *Opt. Mater.* **2010**, *32*, 990–997. https://doi.org/10.1016/j.optmat.2010.01.039

Mazzo, T. M.; Pinatti, I. M.; Macario, L. R.; Avansi Junior, W.; Moreira, M. L.; Rosa, I. L. V.; Mastelaro, V. R.; Varela, J. A.; Longo, E. Europium-doped calcium titanate: Optical and structural evaluations. *J. Alloys Compd.* **2014**, *585*, 154–162. https://doi.org/10.1016/j.jallcom.2013.08.174

Mesquita, W. D.; Oliveira, M. C.; Assis, M.; Ribeiro, R. A. P.; Eduardo, A. C.; Teordoro, M. D.; Marques, G. E.; Godinho Júnior, M.; Longo, E.; Gurgel, M. F. C. Unraveling the relationship between bulk structure and exposed surfaces and its effect on the electronic structure and photoluminescent properties of $Ba_{0.5}Sr_{0.5}TiO_3$: A joint experimental and theoretical approach. *Mater. Res. Bull.* **2021**, *143*, 111442. https://doi.org/10.1016/j.materresbull.2021.111442

Monkhorst, H. J; Pack, J. D. Special points fro Brillouin-zone integretions. *Phys. Rev. B* **1976**, *13*, 5188–5192. https://doi.org/10.1103/PhysRevB.13.5188

Muniz, F. T. L.; Miranda, M. A. R.; Santos, C. M.; Sasaki, J. M. The Scherrer equation and the dynamical theory of X-ray diffraction. *Acta Crystallogr.* **2016**, *A72*, 385–390. https://doi.org/10.1107/S205327331600365X

Navami, D.; Darshan, G. P.; Basavaraj, R. B.; Sharma, S. C.; Kavyashree, D.; Venkatachalaiah, K. N.; Nagabhushana, H. Shape controllable ultrasound assisted fabrication of $CaZrO_3$:Dy^{3+} hierarchical structures for display, dosimetry and advanced forensic applications. *J. Photochem. Photobiol. A Chem.* **2020**, *389*, 112248. https://doi.org/10.1016/j.jphotochem.2019.112248

Nyein, E. E.; Hömmerich, U.; Heikenfeld, J.; Lee, D. S.; Steckl, A. J.; Zavada, J. M. Spectral and time-resolved photoluminescence studies of Eu-doped GaN. *Appl. Phys. Lett.* **2003**, *82*, 1655. https://doi.org/10.1063/1.1560557

Oliveira, M. C.; Gracia, L.; Assis, M.; Rosa, I. L. V.; Gurgel, M. F. C.; Longo, E.; Andrés, J. Mechanism of photoluminescence in intrinsically disordered $CaZrO_3$ crystals: First principles modeling of the excited electronic states. *J. Alloys Compd.* **2017**, *722*, 981–995. https://doi.org/10.1016/j.jallcom.2017.06.052

Oliveira, M. C.; Ribeiro, R. A. P.; Gracia, L.; Lazaro, S. R.; Assis, M.; Oliva, M.; Rosa, I. L. V.; Gurgel, M. F. C.; Longo, E.; Andrés, J. Experimental and theoretical study of the energetic, morphological, and photoluminescence properties of $CaZrO_3$:Eu^{3+}. *CrystEngComm* **2018**, *20* (37), 5519–5530. https://doi.org/10.1039/C8CE00964C

Ortega, P. P.; Rocha, L. S. R.; Cortés, J. A.; Ramirez, M. A.; Buono, C.; Ponce, M. A.; Simões, A. Z. Towards carbon monoxide sensors based on europium doped cerium dioxide. *Appl. Surf. Sci.* **2019**, *464*, 692–699. https://doi.org/10.1016/j.apsusc.2018.09.142

Parchur, A. K.; Ningthoujam, R. S.; Rai, S. B.; Okram, G. S.; Singh, R. A.; Tyagi, M.; Gadkari, S. C.; Tewari, R.; Vatsa, R. K. Luminescence properties of Eu^{3+} doped $CaMoO_4$ nanoparticles. *Dalton Trans.* **2011**, *40* (29), 7595–7601. https://doi.org/10.1039/c1dt10878f

Parchur, A. K.; Ningthoujam, R. S. Behaviour of electric and magnetic dipole transitions of Eu^{3+}, $^5D_0 \rightarrow {}^7F_0$ and Eu–O charge transfer band in Li^+ co-doped YPO_4:Eu^{3+}. *RSC Adv.* **2012**, *2* (29), 10859–10868. https://doi/10.1039/C2RA22144F.

Peipei, D.; Li, G.; Yun, X.; Zhang, Q.; Liu, D.; Lian, H.; Shang, M.; Lin, J. Thermally stable and highly efficient red-emitting Eu^{3+}-doped $Cs_3GdGe_3O_9$ phosphors for WLEDs: non-concentration quenching and negative thermal expansion. *Light Sci. Appl.* **2021**, *10*, 29. https://doi.org/10.1038/s41377-021-00469-x

Pinatti, I. M.; Nogueira, I. C.; Pereira, W. S.; Pereira, P. F. S.; Gonçalves, R. F.; Varela, J. A.; Longo, E.; Rosa, I. L. V. Structural and photoluminescence properties of Eu^{3+} doped α-Ag_2WO_4 synthesized by the green coprecipitation methodology. *Dalton Trans.* **2015**, *44* (40), 17673–17685. https://doi.org/10.1039/C5DT01997D

Pinatti, I. M; Pereira, P. F. S.; Assis, M.; Longo, E.; Rosa, I. L. V. Rare earth doped silver tungstate for photoluminescent applications. *J. Alloys Compd.* **2019**, *771*, 433-447. https://doi.org/10.1016/j.jallcom.2018.08.302

Riul, A.; Fonseca, F. A. A.; Pugina, R. S.; Caiut, J. M. A. Tuned structure of europium-doped $Al2O_3$-ytrium luminescent composites and their spectroscopic behavior. *J. Lumin.* **2021**, *233*, 117925. https://doi.org/10.1016/j.jlumin.2021.117925

Rosa, I. L. V; Oliveira, M. C.; Assis, M.; Ferrer, M.; André, R. S.; Longo, E.; Gurgel, M. F. C. A theoretical investigation of the structural and electronic properties of orthorhombic $CaZrO_3$. *Ceram. Int.* **2015**, *41* (2), 3069–3074. https://doi.org/10.1016/j.ceramint.2014.10.149

Saif, M.; Abdel-Mottaleb, M. S. A. Titanium dioxide nanomaterial doped with trivalent lanthanide ions of Tb, Eu and Sm: Preparation, characterization and potential applications. *Inorganica Chim. Acta* **2007**, *360* (9), 2863–2874. https://doi.org/10.1016/j.ica.2006.12.052

Shimokawa, Y.; Sakaida, S.; Iwata, S.; Inoue, K.; Honda, S.; Iwamoto, Y. Synthesis and characterization of Eu^{3+} doped $CaZrO_3$-based perovskite type phosphors. part II: PL properties related to the two different dominant Eu^{3+} substitution sites. *J. Lumin.* **2015**, *157* (6), 113–118. https://doi.org/10.1016/j.jlumin.2014.08.042

Silva, J. M. P.; Andrade Neto, N. F.; Oliveira, M. C.; Ribeiro, R. A. P.; Lazaro, S. R.; Gomes, Y. F.; Paskocimas, C. A.; Bomio, M. R. D.; Motta, F. V. Recent progress and approaches on the synthesis of Mn-doped zinc oxide nanoparticles: A theoretical and experimental investigation on the photocatalytic performance. *New J. Chem.* **2020**, *44* (21), 8805–8812. https://doi.org/10.1039/D0NJ01530J

Singh, K.; Rajendran, M.; Devi, R.; Vaidyanathan, S. Narrow-band red-emitting phosphor with negligible concentration quenching for hybrid white LEDs and plant growth applications. *Dalton Trans.* **2021**, *50* (14), 4986–5000. https://doi.org/10.1039/D1DT00449B

Smith, M. D.; Connor, B. A.; Karunadasa, H.I. Tuning the Luminescence of Layered Halide Perovskites. *Chem. Rev.* **2019**, *119* (5), 3104–3139. https://doi.org/10.1021/acs.chemrev.8b00477

Song, E.; Zhao, W.; Zhang, W.; Ming, H.; Yi, Y.; Zhou, M. Fluorescence emission spectrum and energy transfer in Eu and Mn co-doped $Ba_2Ca(BO_3)_2$ phosphors. *J. Lumin.* **2010**, *130* (12), 2495–2499. https://doi.org/10.1016/j.jlumin.2010.08.021

Targonska, S.; Szyszka, K.; Rewak-Soroczynska, J.; Wiglusz, R. J. A new approach to spectroscopic and structural studies of the nano-sized silicate-substituted hydroxyapatite doped with Eu^{3+} ions. *Dalton Trans.* **2019**, *48* (23), 8303–8316. https://doi.org/10.1039/C9DT01025D

Tian, X.; Dou, H.; Wu, L. Bi^{3+}-based luminescent thermometry in perovskite-type $CaZrO_3$ phosphor. *J. Mater. Sci. Mater. Electron.* **2020**, *31*, 3944–3950. https://doi.org/10.1007/s10854-020-02942-6

Tiwari, N.; Kuraria, R. K.; Kuraria, S. R. Optical studies of Eu^{3+} doped $CaZrO_3$ phosphor for display device applications. *Optik.* **2015**, *126* (23), 3488–3491. https://doi.org/10.1016/j.ijleo.2015.08.201

Tymiński, A.; Śmiechowicz, E.; Martín, I. R.; Grzyb, T. Ultraviolet- and Near-Infrared-Excitable $LaPO_4$:Yb^{3+}/Tm^{3+}/Ln^{3+} (Ln = Eu, Tb) Nanoparticles for Luminescent Fibers and Optical Thermometers. *ACS Appl. Nano Mater.* **2020**, *3* (7), 6541–6551. https://doi.org/10.1021/acsanm.0c01025

Valenzano, L.; Civalleri, B.; Chavan, S.; Bordiga, S.; Nilsen, M. H.; Jakobsen, S.; Lillerud, K. P.; Lamberti, C. Disclosing the Complex Structure of UiO-66 Metal Organic Framework: A Synergic Combination of Experiment and Theory. *Chem. Mater.* **2011**, *23* (7), 1700–1718. https://doi.org/10.1021/cm1022882

van der Ziel, J. P.; Van Uitert, L. G. Optical Emission Spectrum of Cr^{3+}-Eu^{3+} Pairs in Europium Gallium Garnet. *Phys. Rev.* **1969**, *186*, 332–339. https://doi.org/10.1103/PhysRev.186.332

Vieira, S. A.; Rakov, N.; Araújo, C. B.; Falcão-Filho, E. L. Upconversion luminescence in europium doped Y_2O_3 powder excited by absorption of three, four, and five infrared photons. *Opt. Mater. Express* **2019**, *9* (10), 3952–3961. https://doi.org/10.1364/OME.9.003952

Wu, F.-N.; Yu, H.-J.; Hu, Y.-Y.; Zhang, H.-D.; Zhang, R.; Li, J.; Liu, B.; Wang, X.-P.; Yang, Y.-G.; Wei, L. Effects of slight structural distortion on the luminescence performance in $(Ca_{1-x}Eu_x)WO_4$ luminescent materials. *Luminescence* **2021**, *36* (1), 237–246. https://doi.org/10.1002/bio.3941

Yamaguchi, S.; Kobayashi, K.; Higuchi, T.; Shin, S.; Iguchi, Y. Electronic transport properties and electronic structure of $InO_{1.5}$-doped $CaZrO_3$. *Solid State Ion.* **2000**, *136–137*, 305–311. https://doi.org/10.1016/S0167-2738(00)00408-2

Yang, L.; Kruse, B. Revised Kubelka--Munk theory. I. Theory and application. *J. Opt. Soc. Am. A* **2004**, *21* (10), 1933–1941. https://doi.org/10.1364/JOSAA.21.001933

Zeba, I.; Ramzan, M.; Ahmad, R.; Shakil, M.; Rizwan, M.; Rafique, M.; Sarfraz, M.; Ajmal, M.; Gillani, S. S. A. First-principles computation of magnesium doped $CaZrO_3$ perovskite: A study of phase transformation, bandgap engineering and optical response for optoelectronic applications. *Solid State Commun.* **2020**, *313* (4), 113907. https://doi.org/10.1016/j.ssc.2020.113907

Zhang, H.; Fu, X.; Niu, S.; Xin, Q. Synthesis and photoluminescence properties of Eu^{3+}-doped $AZrO_3$ (A=Ca, Sr, Ba) perovskite. *J. Alloys Compd.* **2008**, *459* (1–2), 103–106. https://doi.org/10.1016/j.jallcom.2007.04.259

Zhang, J.; Cai, G.; Wang, W.; Ma, L.; Wang, X.; Jin, Z. Tuning of Emission by Eu^{3+} Concentration in a Pyrophosphate: the Effect of Local Symmetry. *Inorg. Chem.* **2020**, *59* (4), 2241–2247. https://doi.org/10.1021/acs.inorgchem.9b02949

Zheng, H.; Reaney, I. M.; Csete de Györgyfalva, G. D. C.; Ubic, R.; Yarwood, J.; Seabra, M. P.; Ferreira, V. M. Raman spectroscopy of $CaTiO_3$-based perovskite solid solutions. *J. Mater. Res.* **2004**, *19*, 488–495. https://doi.org/10.1557/jmr.2004.19.2.488

Zhou, Q.; Fang, Y.; Li, J.; Hong, D.; Zhu, P.; Chen, S.; Tan, K. A design strategy of dual-ratiomentric optical probe based on europium-doped carbon dots for colorimetric and fluorescent visual detection of anthrax biomarker. *Talanta* **2021**, *222*, 121548. https://doi.org/10.1016/j.talanta.2020.121548

ISSN: 1678-4618
DOI: 10.26850/1678-4618eqj.v47.1SI.2022.p90-104